THE ASTROPHYSICAL JOURNAL, 436:741–748, 1994 December 1

HIGH-VELOCITY SULFUR MONOXIDE EMISSION FROM PROTOSTELLAR OUTFLOWS

LAWRENCE M. CHERNIN
Center for Astrophysics; and Department of Astronomy, University of California, Berkeley, CA 94720;
chernin@ucbast.berkeley.edu

COLIN R. MASSON
Center for Astrophysics, MS 78, 60 Garden Street, Cambridge, MA 02138;
masson@cfa.harvard.edu

AND

GARY A. FULLER
NRAO, 949 North Cherry Avenue, Tucson, AZ 85721-0665;
gfuller@nrao.edu

Received 1993 November 3; accepted 1994 May 31

ABSTRACT

We have mapped the $J_N = 2_3$–1_2, 3_2–2_1 and 6_5–5_4 transitions of SO and the $J = 5$–4 transition of SiO in nine regions containing protostellar molecular outflows. We find that, in general, the spatial pattern of the SO emission and shape of the line profiles is different for each transition. In the quiescent gas, the SO emission is widespread in the ambient clouds, but $J_N = 2_3$–1_2 and $J_N = 3_2$–2_1 emission is relatively weak in the warm, dense cores around the young stars, while the $J_N = 6_5$–5_4 emission is found to be strongest in the cores. In the outflowing gas, the SO 6_5–5_4 line is detected toward the outer parts of the CO lobes and shows high-velocity (HV: 5–32 km s^{-1}) wings, while the SO $J_N = 3_2$–2_1 and $J_N = 2_3$–1_2 emission is not detected. SiO $J = 5$–4 shows similar HV emission to SO $J_N = 6_5$–5_4, but little emission from the quiescent gas. In general, SO and SiO emission from the outflow does not resemble maps or line profiles of CO, CS, NH_3, or HCO^+.

These results give further support that lines of SO and SiO can be very useful as specific tracers of shocked gas in outflows. The observations presented here are not easily explained with the current shock models.

Subject headings: ISM: jets and outflows — ISM: molecules — molecular processes — shock waves — stars: pre–main-sequence

1. INTRODUCTION

Protostellar molecular outflows are believed to be driven by highly supersonic jets (Masson & Chernin 1993, hereafter MC; Raga & Cabrit 1993; Stahler 1993), but there is little observational data that directly traces the shocked ambient molecular gas. While CO is the most sensitive tracer of the mass in the outflow, its chemistry is relatively insensitive to nondissociative ($T < 10^4$ K) shocks (Mitchell 1984) which are the predominant type of shock in these outflows (cf. MC). On the other hand, the SO and SiO chemistry is strongly affected at the temperatures produced in this kind of shock (Mitchell 1984; Hartquist, Oppenheimer, & Dalgarno 1980; Pineau des Forêts et al. 1993, hereafter PDFRSF). However, there are few outflow observations that can be directly compared with these models (e.g., Bachiller, Martin-Pintado, & Fuente 1991; Martin-Pintado, Bachiller, & Fuente 1992; Chernin & Masson 1993, hereafter CM).

Millimeter wavelength SO emission is often found in quiescent molecular cores (Gottlieb et al. 1978; Rydbeck et al. 1980) where the density is high enough ($> 10^5$ cm^{-3}) for collisional excitation. However, the spatial distribution of SO emission can be quite different from that of tracers of the dense gas such as CS and C_3H_2 (Swade 1989), indicating either unusual excitation or strong abundance variations. SO and SiO emission has also been found in protostellar outflows from massive star-forming regions such as Orion-IRC 2 and Ceph A (Welch et al. 1981; Plambeck et al. 1982; Martin-Pintado, Bachiller, & Fuente 1992), where the SO abundance is enhanced by several orders of magnitude over that in quiescent material. Recent observations showed that there is unusually strong HV SO $J_N = 6_5$–5_4 and SiO emission from the NGC 2071 outflow and also that the spatial and velocity distribution of SO and SiO emission is quite different from that of CO (CM). The differences in SO and SiO relative to CO were attributed to abundance enhancements caused by shocks rather than excitation differences.

In the present paper, we present measurements of two other transitions of SO, $J_N = 2_3$–1_2, and $J_N = 3_2$–2_1, made in order to understand the excitation of SO, the prevalence of SO and SiO enhancements in outflows, and the differences from CO and other molecules. In § 2 we present the parameters of the SO observations obtained with the Caltech Submillimeter Observatory and Five College Radio Astronomy Observatory. In § 3 the basic results are shown and a comparison is made between different SO transitions and the CO in molecular outflows. In § 4 we consider the SO excitation and the implications of our results for shock chemistry and the dynamics of outflows.

2. OBSERVATIONS

Lists of our observed sources and lines are presented in Tables 1 and 2, respectively. We chose a sample of nine of the most well-known outflows from low- to intermediate-mass stars and mapped the SO emission in large regions around the outflows with the QUARRY 3 mm receiver system of the Five College Radio Astronomy Observatory (FCRAO).[1] The

[1] The FCRAO is operated with support from the National Science Foundation (contract AST 85-12903) and the commonwealth of Massachusetts with permission of the Metropolitan District Commission.

TABLE 1

SOURCES PROPERTIES

Source	R.A. (1950)	Decl. (1950)	V_{LSR} (km s^{-1})	SO Lines Observed J_N
L1448C	$3^d22^m34\overset{s}{.}4$	30°33′35″	4.5	3_2–2_1
NGC 1333-IRAS 4	3 26 05	31 03 13	7.0	2_3–1_2, 3_2–2_1, 6_5–5_4
IRAS 03282+3035	3 28 15.2	30 35 14	7.0	3_2–2_1, 6_5–5_4
L1551	4 28 44	18 01 51	6.0	3_2–2_1
NGC 2024	5 39 12.6	−1 51 00	10.0	3_2–2_1, 6_5–5_4
NGC 2071	5 44 30	0 20 40	10.0	2_3–1_2, 3_2–2_1, 6_5–5_4
NGC 2264C	6 38 26	9 32 00	7.5	3_2–2_1, 6_5–5_4
NGC 2264D	6 38 19	9 37 32	7.5	3_2–2_1
LkHα 234	21 41 3.2	65 52 42	−10.0	3_2–2_1

TABLE 2

OBSERVED LINES

Transition	Frequency (GHz)	T_u (K)	Telescope	Beam Size (FWHM)
SO $J_N = 3_2$–2_1	99.2999	9	FCRAO	54″
SO $J_N = 2_3$–1_2	109.2521	16	FCRAO	50
SiO $J = 5$–4	217.1049	21	CSO	33
SO $J_N = 6_5$–5_4	219.9491	35	CSO	33

QUARRY receiver simultaneously observes a 3 × 5 grid with an average system temperature in each receiver of 300–500 K. The observations were performed in 1992 December and 1993 February. The beam size is 54″ (FWHM) at 100 GHz, with a main beam efficiency of 0.50–0.55. Pointing errors were less than 7″. We mapped the SO $J_N = 3_2$–2_1 line in all sources but the SO $J_N = 2_3$–1_2 line is much weaker than $J_N = 3_2$–2_1 and was mapped in only two of the strongest sources (NGC 1333 and NGC 2071).

In 1992 October and 1993 February we observed the SO $J_N = 6_5$–5_4 line at the Caltech Submillimeter Observatory (CSO)[2] but could cover only a much smaller area on the sky than the observations with the QUARRY system. The observations were performed in a double-sideband mode with SiO $J = 5$–4 in the lower sideband and SO $J_N = 6_5$–5_4 and ^{13}CO (2–1) in the upper sideband. Careful attention was given to match the sideband gains by measuring line strengths in Orion-IRC 2 and comparing with line catalogs (cf. Sutton et al. 1985). Typical system temperatures were 500 K and the main beam efficiency is 0.72. Pointing errors were typically less than 5″.

Both the FCRAO and CSO observations were performed in a position switching mode, with off positions chosen to avoid most of the emission from the ambient cloud. Typical off positions ranged from 5′ to 20′. The spectra and maps are presented as T_A^* with no corrections for source size and beam pattern.

3. RESULTS

3.1. *The* CO *Outflow and the* SO $J_N = 3_2$–2_1 *Emission*

Maps of the $J_N = 3_2$–2_1 emission from the sample are shown in Figure 1, with overlays of the outline (lowest significant contour) of the CO outflow superposed (dashed line). Widespread SO emission is detected in all the outflow regions, but there is little obvious connection between the SO emission and the CO outflows. The observed SO $J_N = 3_2$–2_1 line widths are narrow (see below), indicating that the SO $J_N = 3_2$–2_1 emission arises predominantly from the quiescent ambient gas. In L1448, IRAS 03282+3035, L1551, NGC 2071, NGC 2024 and NGC 2264D the SO $J_N = 3_2$–2_1 emission is very weak or even absent in at least one of the two lobes of the outflow. In L1551 and IRAS 03282+3035, the $J_N = 3_2$–2_1 SO emission appears to be concentrated at the edges of the lobes.

3.2. *Comparison of Maps of* SO $J_N = 2_3$–1_2, $J_N = 3_2$–2_1, *and* $J_N = 6_5$–5_4 *Emission*

$J_N = 6_5$–5_4 was mapped in NGC 2071, NGC 2024, NGC 2264D, NGC 1333, and part of the IRAS 03282 region, and $J_N = 2_3$–1_2 was mapped in NGC 2071 and NGC 1333. The beam sizes are somewhat different for the transitions, and this will affect most of the extended structure so we concentrate the discussion on the gross features in the maps.

Figures 2*a* and 2*b* show maps of the integrated emission from these lines in the NGC 1333 and NGC 2071 regions. In general, the peaks of the maps in the different lines do not coincide. For example, in NGC 1333 the $J_N = 6_5$–5_4 peak at (−0.6, 1.6), which corresponds to the middle of the blue lobe of the HH 7-11 (IRAS 3) outflow (Liseau, Sandell, & Knee 1988), is not in the $J_N = 2_3$–1_2 map. On the other hand, the nearby peak in the $J_N = 3_2$–2_1 map (0, 1.6) corresponds to a position beyond the end of the blue lobe. In NGC 2071 the $J_N = 2_3$–1_2 and $J_N = 3_2$–2_1 maps are fairly similar in that they both show the same peaks, but the ridge of NW-SE emission does not show up well in the $J_N = 2_3$–1_2 transition. The area mapped in $J_N = 6_5$–5_4 was only slightly larger than the CO outflow, but the emission is considerably different from the other SO lines, with strong emission from positions toward the ends of the outflow as well as the central core at (0, 0).

Figures 3*a* and 3*b* compare the $J_N = 3_2$–2_1 and $J_N = 6_5$–5_4 emission distributions in NGC 2024 and NGC 2264C. The distributions of SO emission in these two lines are more similar in these regions than those shown in Figure 2, however the $J_N = 6_5$–5_4 peak at FIR 2 (−0.4, 1.5) is not evident in $J_N = 3_2$–2_1. The general positional orientation of the extended emission in NGC 2024 is comparable in both the $J_N = 2_3$–1_2 and $J_N = 3_2$–2_1 transitions, indicating that they are both tracing the same ridge of dense gas that has been in several other lines (e.g., Russell, Hills, & Padman 1987). In NGC 2264C the NW-SE ridge of emission to the north of the source is seen in both lines.

3.3. *Spectra*

Spectra at the peaks of the SO $J_N = 6_5$–5_4 emission are shown in Figure 4. The $J_N = 2_3$–1_2 lines were weaker than the $J_N = 3_2$–2_1 lines and have not been shown here. The clear

[2] The CSO is operated by the California Institute of Technology under funding from the NSF, contract number AST 90-15755.

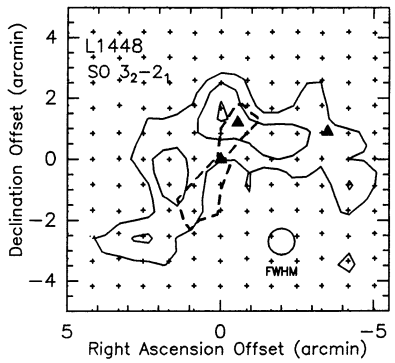

FIG. 1*a*

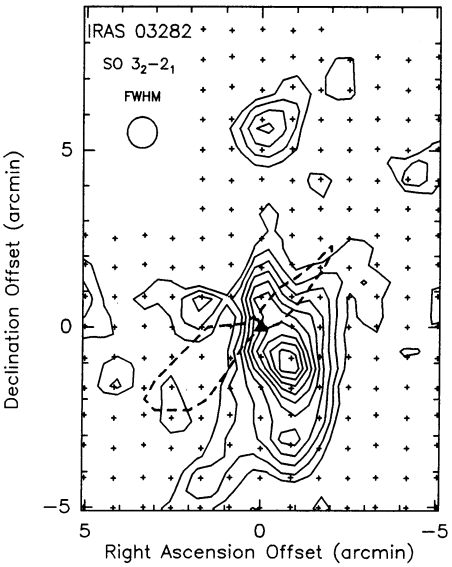

FIG. 1*b*

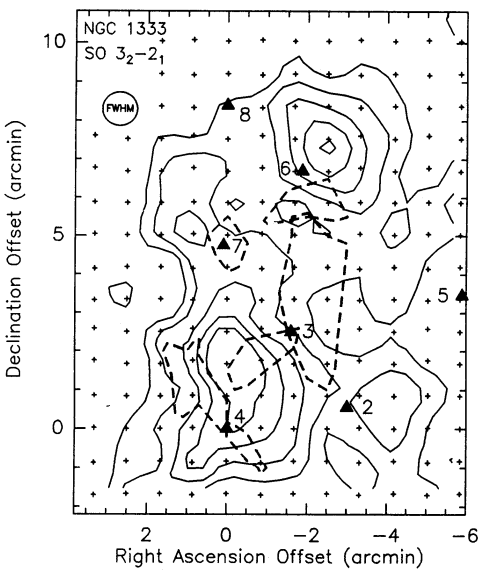

FIG. 1*c*

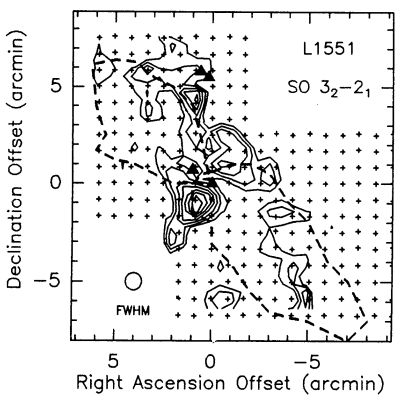

FIG. 1*d*

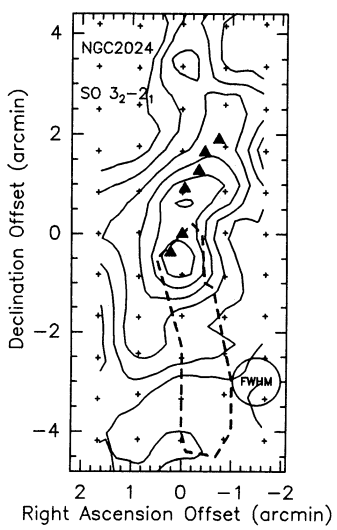

FIG. 1*e*

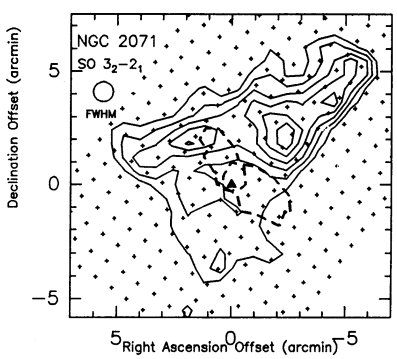

FIG. 1*f*

FIG. 1.—Comparison of the outline of the CO $J = 1$–0 emission (*dashed outline*) from protostellar outflows and the SO $J_N = 3_2$–2_1 emission (*solid outline*). The crosses represent the pointing centers and triangles represent the major infrared sources. *IRAS* sources are numbered in NGC 1333. The numerous IR sources in NGC 2071 (Strom et al. 1976) have been omitted. Contour levels are 3 σ which is given for each region and the CO data is referenced. Sources: (*a*) L1448C, 0.2 K km s^{-1} (Bachiller et al. 1990), (*b*) IRAS 03282+3035, 0.1 K km s^{-1} (Bachiller 1991b), (*c*) NGC 1333, 0.5 K km s^{-1} (Liseau et al. 1988; G. Blake, private communication), (*d*) L1551, 0.12 K km s^{-1} (Snell & Schloerb 1985), (*e*) NGC 2024, 0.5 K km s^{-1} (Richer, Hills, & Padman 1992), (*f*) NGC 2071, 0.5 K km s^{-1} (Snell et al. 1984), (*g*) NGC 2264C, 1 K km s^{-1} (Margulis et al. 1988), (*h*) NGC 2264D, 1 K km s^{-1} (Margulis et al. 1988), and (*i*) LKHα 234, 0.3 K km s^{-1} (Edwards & Snell 1983). In general, there is no correlation between the CO outflow and the SO $J_N = 3_2$–2_1 emission.

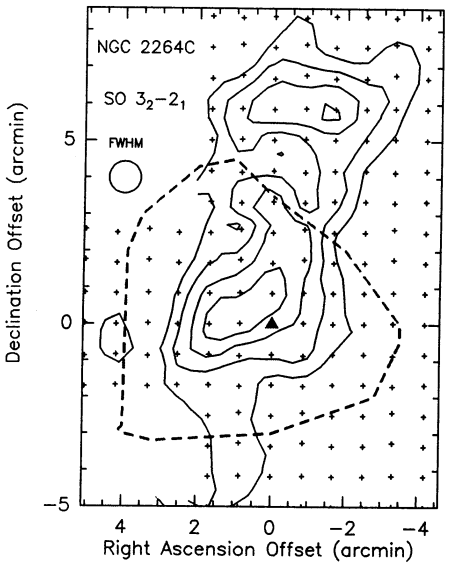

FIG. 1*g*

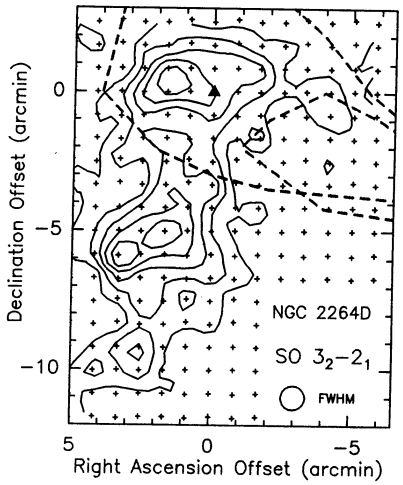

FIG. 1*h*

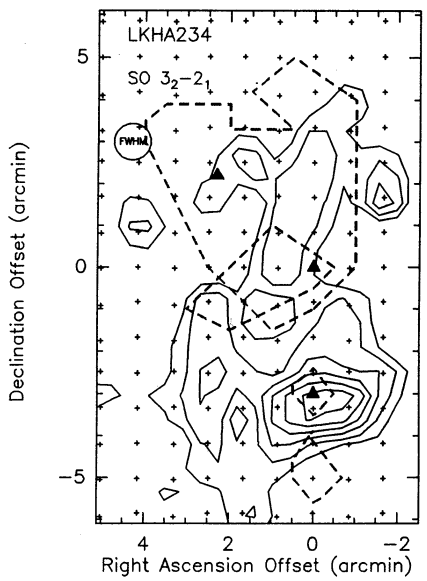

FIG. 1*i*

difference between the $J_N = 6_5$–5_4 and $J_N = 3_2$–2_1 spectra is in the existence of HV wings in the $J_N = 6_5$–5_4 spectra. This is not a sensitivity effect since the line widths at FWHM are also much larger in the $J_N = 6_5$–5_4 than the $J_N = 3_2$–2_1 line. It is unlikely to be result of beam dilution of the HV wings relative to more extended quiescent gas, since the ratio of (beam area/efficiency) for the two telescopes is only 4 while a lower limit to the intensity is 10 in NGC 1333 IRAS 2, 4, and NGC 2024. In the extreme case of IRAS 03282+3035 (2.8, −2) the $J_N = 6_5$–5_4 line shows only HV emission, with no detected emission from the quiescent gas. The velocity range of the $J_N = 6_5$–5_4 emission is limited by the noise level and Table 3 shows these ranges as determined from our data. At the 100 mK level most of the spectra in Figure 4 show a similar velocity range of 11–13 km s^{-1}. For NGC 2071 (0.75, 1.1), which had the lowest noise, SO emission was detected up to 32 km s^{-1} (1 σ) from the cloud velocity. In contrast, the $J_N = 2_3$–1_2 and $J_N = 3_2$–2_1 lines have maximum widths of a few kilometers per second.

3.4. SiO

In addition to SO $J_N = 6_5$–5_4, we obtained simultaneous observations of the SiO $J = 5$–4 line in the other sideband of the receiver. Figure 5 shows that the HV SO $J_N = 6_5$–5_4 spectra and HV SiO $J = 5$–4 spectra have a similar shape in all sources except NGC 2024, where we did not detect any SiO emission. Figure 6 shows a comparison of these lines at NGC 2071 (0.75, 1.1) with ^{13}CO. The SiO and SO line shapes are similar, but quite different from the sharply decreasing CO profile.

TABLE 3

SO PEAK BRIGHTNESS AND VELOCITY RANGES FOR HV SOURCES

SOURCE	T_A^{*}[a] (K)			σ_{rms} (mK)	$\lvert V_{1\sigma} - V_{LSR}\rvert$ (km s^{-1})	$\lvert V_{100\,mK} - V_{LSR}\rvert$ (km s^{-1})
IRAS 03282+3035(2.8, −2)	<0.1	...	0.5	26	17	10
NGC 1333 IRAS 2(1, −0.25)	0.9	0.2	1.0	50	18	13
NGC 1333 IRAS 4	1.5	0.5	1.4	27	15	12
NGC 2024 FIR 6	1.4	...	4.7	40	24	13
NGC 2071 (0.75, 1.1)	0.3	0.1	0.3	18	32	12
NGC 2264C (0, 0.5)	1.5	...	1.3	40	14	11

[a] Peak $J_N = 3_2$–2_1, $J_N = 2_3$–1_2, $J_N = 6_5$–5_4 antenna temperature in a 1 km s^{-1} wide channel.

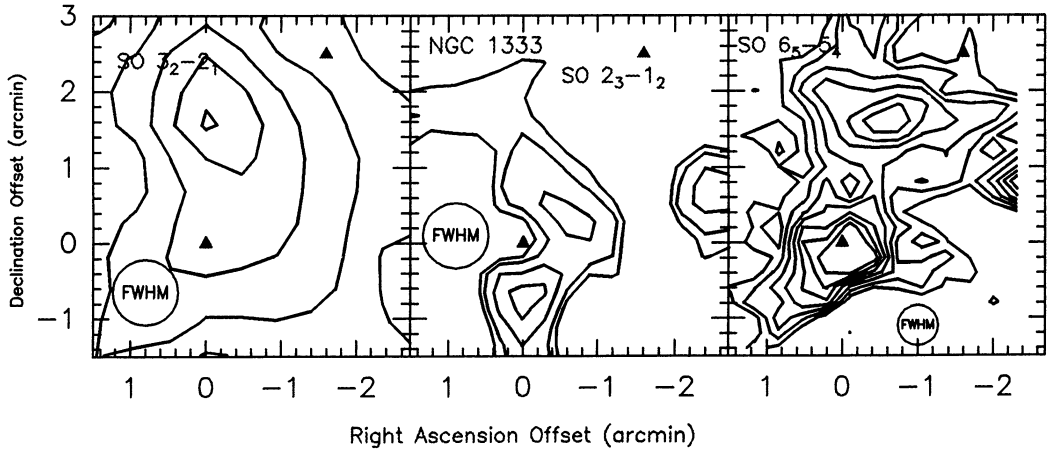

FIG. 2a

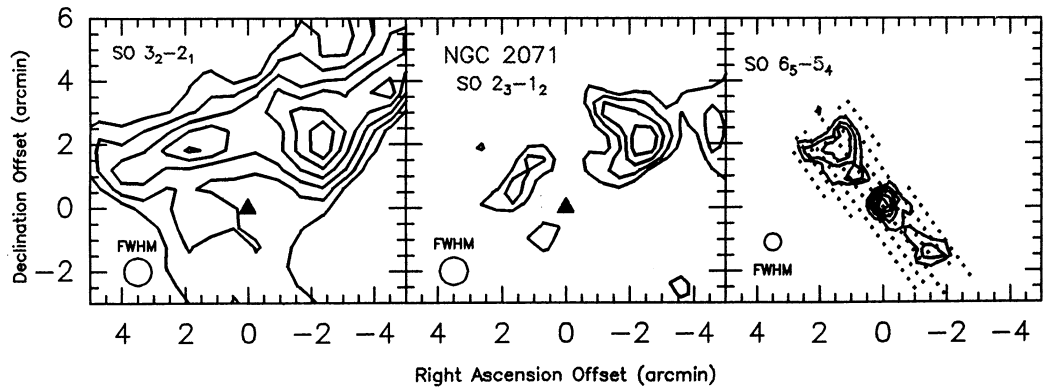

FIG. 2b

FIG. 2.—Comparison of the three SO transitions in NGC 1333 and NGC 2071 in (*a*) and (*b*), respectively. The beam FWHM is shown in each map. Note the differences in the emission patterns is not a beam area effect and the emission regions of the three transitions is clearly different. The *IRAS* sources are marked with triangles.

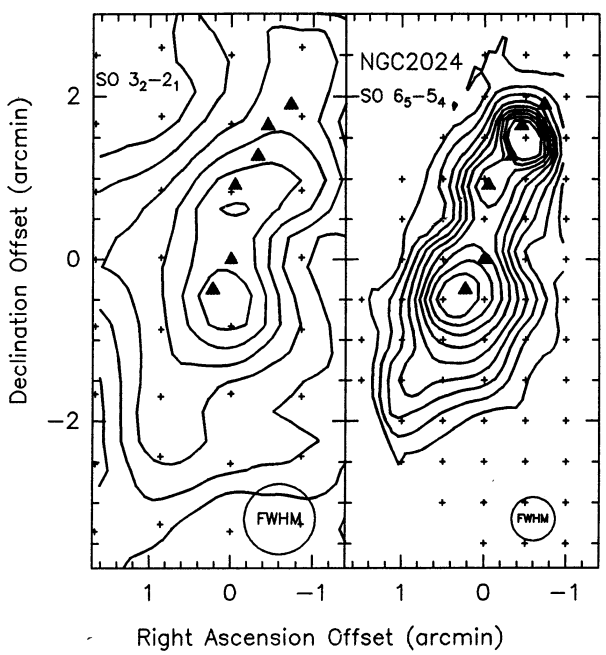

FIG. 3a

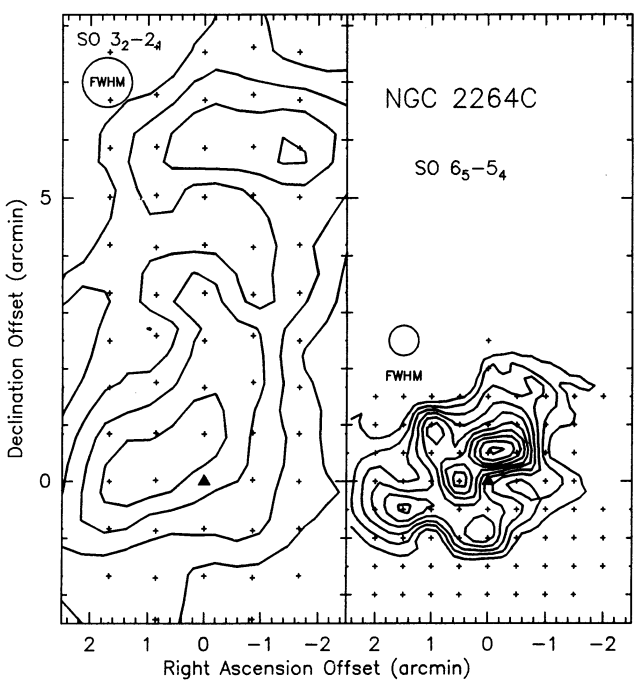

FIG. 3b

FIG. 3.—A comparison of the $J_N = 3_2$–2_1 and $J_N = 6_5$–5_4 emission in NGC 2024 and NGC 2264C is shown in (*a*) and (*b*) respectively. Note the clumpiness of the $J_N = 6_5$–5_4 emission. The FIR sources are marked with asterisks and do not correspond to the SO peaks.

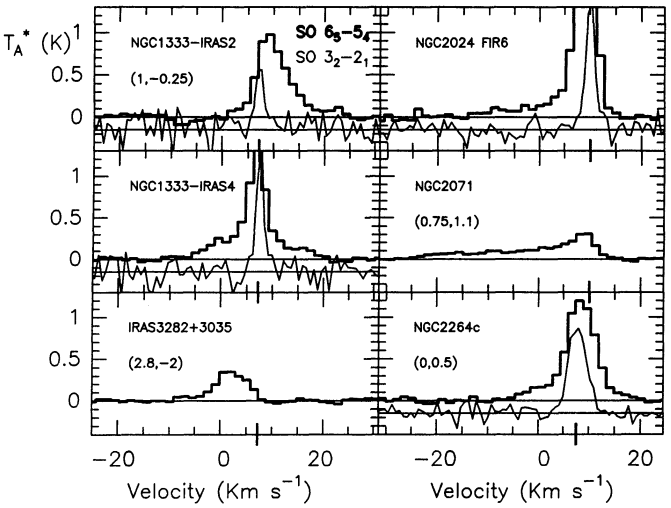

FIG. 4.—SO spectra at selected positions in the outflows which show HV $J_N = 6_5$–5_4 emission. The $J_N = 6_5$–5_4 transition shows HV wings while the $J_N = 3_2$–2_1 emission originates primarily from quiescent gas. The HV emission region is unresolved by the 33″ beam. Note that for IRAS 2, the offset (1, −0.25) is relative to the IRAS 2 source and not the position in Table 1 (IRAS 4).

3.5. *Individual Sources*

L1448C.—The spatial distribution of the SO $J_N = 3_2$–2_1 emission from L1448 is quite different from the NH_3 but similar to the CS emission maps presented by Bachiller et al. (1990). The NH_3 emission is strongly peaked near the *IRAS* source 1′.5 to the north of L1448C, while the $J_N = 3_2$–2_1 SO and CS emission is more diffuse. The NH_3 peak at L1448C is very weak in SO $J_N = 3_2$–2_1 and $J_N = 6_5$–5_4. Although HV (>60 km s^{-1}) SiO emission has been detected in L1448 by Bachiller et al. (1991a), we did not detect SO $J_N = 6_5$–5_4 or SiO (5–4) emission from L1448 to a level of less than 0.1 K (3 σ).

IRAS 03282+3035.—The NH_3 (1, 1) emission from IRAS 03282+3035 peaks very close to the position of the *IRAS* source at the center of the bipolar flow (cf. Bachiller et al. 1991b). However, there is relatively weak SO emission at this position, and SO $J_N = 3_2$–2_1 peaks 1′.5 to the southwest. A few

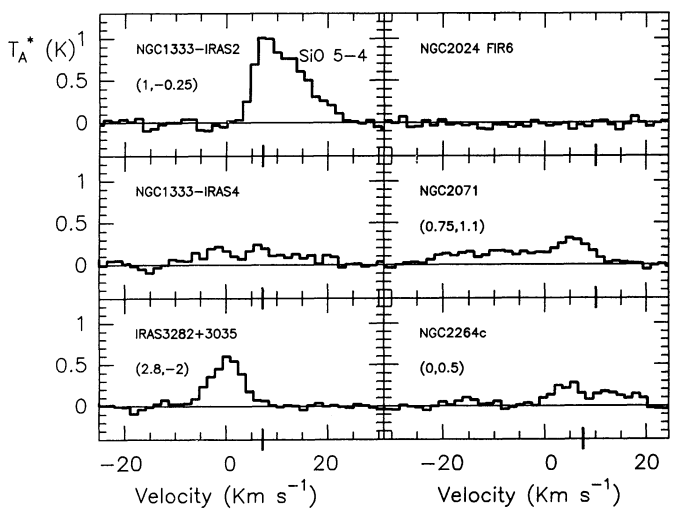

FIG. 5.—SiO J = 5–4 emission at the same positions as shown in Fig. 4. Note the similarity in the line shapes of the HV SiO with those of SO.

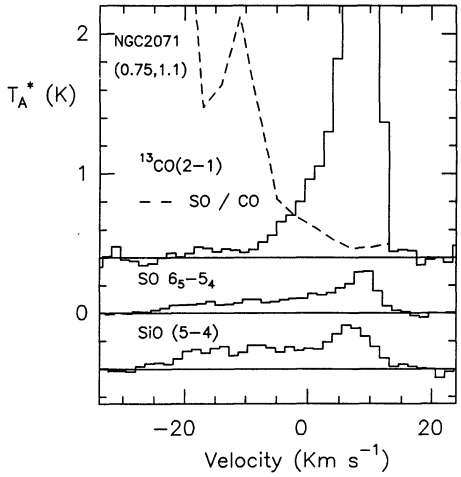

FIG. 6.—SO, SiO, and ^{13}CO spectra in NGC 2071. Note that the SO and SiO HV line profiles are much flatter than that of CO and therefore the SO(SiO)/CO line ratio increases with velocity. This suggests that the SO(SiO) may be produced in HV shocks in which the CO is relatively uneffected.

strips along the outflow axis were mapped in $J_N = 6_5$–5_4 but emission was only found at the ends of the CO lobes.

NGC 1333.—The CS map of NGC 1333 presented by Liseau et al. (1988) shows a single peak in the region covered by the SO maps (Fig. 2*a*). This CS peak is located at about (−1.5, 0.5) and is close to a local minimum in the SO emission in all three lines. The ^{13}CO emission pattern (Liseau et al. 1988) is quite similar to that of the CS emission and we conclude that SO does not trace the density structure of this cloud. We detected SiO emission from the highly collimated bipolar outflow from IRAS 4 (Blake, private communication), similar to that in the L1448 outflow (Bachiller et al. 1991a).

L1551.—The brightest SO $J_N = 3_2$–2_1 emission from L1551 is at (1, −1) is close to a low-velocity redshifted CO peak (Moriarty-Schieven & Snell 1988). The SO emission from the northern edge of the CO lobes coincides with the low-velocity CO shell (Snell & Schloerb 1985), although there is some weak SO emission to the southwest that lies in the center of the CO lobe.

NGC 2024.—The NH_3 emission from NGC 2024 has peaks below FIR 6 and between FIR 2 and 3 (Gaume, Johnston, & Wilson 1992). These NH_3 peaks are similar to the peaks in the SO $J_N = 6_5$–5_4 emission. On the other hand, the HCO+ maps of Russell et al. (1987) and Lis, Carlstrom, & Phillips (1991) look more like the SO $J_N = 3_2$–2_1 map, with weak emission from the northern SO $J_N = 6_5$–5_4 peak. The 1.3 mm continuum emission has strong peaks at FIR 3, 4, 5, and 6, but a 30″ resolution map at 350 μm is very similar to the SO $J_N = 6_5$–5_4 map (Mezger et al. 1988). HV HCO+ emission was detected at FIR 6 by Lis et al. (1991).

NGC 2071.—The CS, HCN, HCO^+, and NH_3 emission in NGC 2071 are all strongly peaked on the IR cluster (Kitamura et al. 1990) in contrast to the SO $J_N = 2_3$–1_2 and $J_N = 3_2$–2_1 emission which have a local minimum there. The elongation of the NH_3 ridge is at a position angle of 150° but the $J_N = 3_2$–2_1 emission extends over a position angle of 110°–130°. A ridge at a position angle of 110°–150° has also been seen in ^{13}CO (White & Phillips 1981).

NGC 2264C, D, and LKHα 234.—The integrated CO emission from NGC 2264 (Margulis, Lada, & Snell 1988; Bechis et al. 1978) shows a similar morphology to the $J_N = 3_2$–2_1 SO

emission. Unlike most of the sources discussed above, in this case, the $J_N = 3_2$–2_1 SO emission traces the same gas as CO in these regions.

In summary, emission from the lower transitions of SO is spread over the clouds, but it often shows a minimum at the density peak as indicated by other molecules. Emission from the lower transitions are generally absent in the outflowing gas. $J_N = 6_5$–5_4 emission is found in outflows, but in relatively compact regions, toward the central source and at the ends of the lobes, rather than being spread throughout the lobes. In general, the SO maps do not look like those of such molecules as HCO^+, NH_3 and CS.

4. DISCUSSION

4.1. *Excitation of* SO

The three SO lines $J_N = 3_2$–2_1, $J_N = 2_3$–1_2, and $J_N = 6_5$–5_4 sample a range of excitation, with upper state energies of 9, 16 and 35 K, respectively. The density for thermalization of the lower energy lines is near 10^6 cm^{-3} (cf. Welch et al. 1981) and is similar to that of $J_N = 6_5$–5_4, 2×10^6 cm^{-3} (based on an A value of 1.6×10^{-4} s^{-1}). The high excitation level (6_5) cannot be easily thermalized in extended regions of the lobes, such as seen in Figure 1, because most of the material is at a density that is two to three orders of magnitude below the critical density for this level (cf. Bally & Lada 1983). This is an argument in favor of the SO emission arising from compressed shocked regions.

Figure 7 shows a rotation diagram (cf. Cummins, Linke, & Thaddeus 1986; Sutton et al. 1991) of the HV SO emission near NGC 1333–IRAS 2 integrated over 8–23 km s^{-1}, made on the assumption that the HV emission is optically thin. The excitation shows a strong departure from LTE in the sense that the $J_N = 6_5$–5_4 emission is too strong, compared with the lower energy transitions. An infinite temperature would produce a horizontal line on the diagram in Figure 7. For a plausible temperature of 25 K in LTE, the HV $J_N = 6_5$–5_4 intensity of 10 K km s^{-1} would imply a $J_N = 3_2$–2_1 intensity of 3.7 K km s^{-1} for an unresolved source, significantly greater than our 3 σ limit of 2.1 K km s^{-1}.

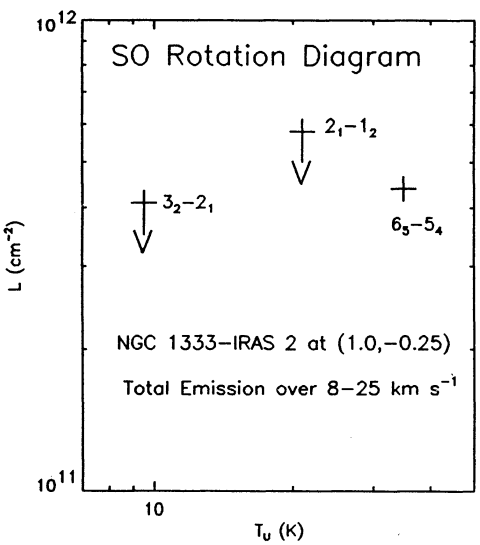

FIG. 7.—Rotation diagram of the three SO transitions in NGC 1333 at (1.0, −0.25) from IRAS 2. The quantity on the y-axis is related to the column density of the gas (Sutton et al. 1992; Cummins et al. 1986). The line emission has been integrated over the HV wing in $J_N = 6_5$–5_4 (8–23 km s^{-1}) and the antenna temperatures have been corrected by the main beam efficiency and beam size. The strong $J_N = 6_5$–5_4 emission relative to $J_N = 3_2$–2_1 and $J_N = 2_3$–1_2 is unlikely to be due to gas in LTE or to subthermal excitation, and further measurements are needed to determine the excitation. Note an error in figure: 2_1–1_2 should read 2_3–1_2.

The unusual line ratios are also found in several of the outflows (NGC 2071, NGC 2024–FIR 2 and NGC 1333–IRAS 4), although the low-velocity gas in the core does not show this effect. One possible explanation is that the HV emission arises from very compact clumps in which the lower transitions are optically thick, although we note that this would not easily explain the SO emission from SGR B2 (Cummins et al. 1986; Sutton et al. 1991) unless the maximum optical depth is near transitions with $T_{upper} = 80$ K. More detailed measurements are needed in order to determine the nature of the SO excitation.

4.2. *Spatial and Velocity Distribution of* SO *and* SiO

From the maps and spectra shown above it is clear that the $J_N = 2_3$–1_2 and $J_N = 3_2$–2_1 emission is not strong in the outflow lobes, but this does not imply that there is an underabundance of SO in the outflow. The $J_N = 6_5$–5_4 spectra show HV wings while the other two lines do not, and thus $J_N = 6_5$–5_4 may be a better tracer of the outflow. The similarities of line profiles and spatial distribution suggest that SiO $J = 6$–5 and SO $J_N = 6_5$–5_4 are both tracing the same gas. The HV SiO lines show a similar shape to SO, in contrast to the sharply decreasing CO line profile which is a characteristic of outflows (MC). The high-velocity SiO in L1448 (Bachiller et al. 1991a) is strongly enhanced and has similar line shapes over several SiO transitions ($J = 2$–1, $J = 3$–2 and $J = 5$–4).

4.3. *Comparison with Shock Models*

Calculations showing the abundance of SO in the vicinity of shocks have been recently presented by PDFRSF. Two important observations constrain the PDFRSF shock models: the HV SO is spatially unresolved (<33″) and enhanced in abundance. Although the abundance of HV SO is very difficult to determine from the data presented here, Figure 6 clearly shows that there is a gradient in the SO/CO emission ratio which more likely traces an abundance effect than an excitation effect. An LTE estimation of the abundances (CM) indicates that the SO is moderately ($\times 10$) enhanced in the HV gas. The abundance may be even higher if the excitation is subthermal.

Now we consider the implications of this enhancement for the shock models. Figure 8*b* of PDFRSF shows that there is a region of enhanced HV SO abundance very close to the shock front, from 0.01 to 0.08 pc, then a depletion region, and a second enhanced SO region 0.2–0.4 pc behind the shock front. The dip in the SO abundance between these regions is where SO is efficiently converted into SO_2, but the SO_2 is ultimately broken to S by reactions with H_3^+ and cosmic rays. Then S can react with oxygen to form the second SO peak. Our $J_N = 6_5$–5_4 observations show the HV SO originates from a region smaller than 33″ which corresponds to 0.08 pc at 400 pc. We do not detect HV SO emission from the posited second region of enhanced SO abundance. This is not simply an effect of comparing our data with a simple planar shock because the "sandwich"'structure is not evident at any velocity in the outflows. Insufficient excitation is unlikely because we have observed three transitions with a range of excitation. Alternatively the initial conditions for the shock may be different than in the model. Another possibility is that the wide-scale $J_N =$

3_2–2_1 and $J_N = 2_3$–1_2 SO emission may be related to this post-shock chemical evolution in that SO is initially produced very close to the (nonplanar) shock front but slowly mixes in with the bulk flow at much lower velocities. More sophisticated models are needed to test this possibility. Observations of chemically related species such as SO_2 and H_2S would also be very helpful.

4.4. *Connection to Outflow Models*

The relatively flat SO and SiO HV line profiles indicate that a range of shock speeds must be present in the emission region and the similarity of the SO and SiO line profiles indicates that a similar mechanism gives rise to this emission. A bow shock driven by a collimated jet has high velocities at its apex but much lower velocities in the extended wings of the bow. MC have developed such a model for the swept-up gas and thus the observations presented here can provide useful constraints on the gas dynamics close to the bow shock. A model of jet-driven molecular outflows has also been proposed by Raga & Cabrit (1993). The basic differences between these models is in the long-term evolution (>1000 yr) of the shocked gas. The lower velocity SO emission, that is not associated with cores (i.e., as in NGC 1333) may be tracing this evolution, but the details cannot be sorted out with the current models.

There can be also useful information on the direct interaction between the jet and the ambient medium. The size of the bow shock region that has highly supersonic velocities (i.e., >25 km s^{-1} in a 60 km s^{-1} bow shock) can be estimated from the simulations of Chernin et al. (1994) to be smaller than a few jet radii. Thus since the jet diameters are usually smaller than 10^{16} cm, the velocity structure of the emission region would be unresolved even with a 8″ (at 400 pc) beam, requiring interferometric measurements.

We would like to thank Mark Heyer for help with the FCRAO observations, Peter Barnes for assistance with the FCRAO data reduction software, and Karl Menten for helpful comments on the SO excitation. G. A. F. acknowledges the support of a National Radio Astronomy Observatory Jansky Fellowship.

REFERENCES

Bachiller, R., Cernicharo, J., Martin-Pintado, J., Tafalla, M., & Lazareff, B. 1990, A&A, 231, 174
Bachiller, R., Martin-Pintado, J., & Fuente, A. 1991a, A&A, 243, L21
Bachiller, R., Martin-Pintado, J., & Planesas, P. 1991b, A&A, 231, 176
Bally, J., & Lada, C. J. 1983, ApJ, 265, 824
Bechis, K. P., Harvey, P., Campbell, M. F., & Hoffmann, W. F. 1978, ApJ, 226, 439
Chernin, L. M., & Masson, C. R. 1993, ApJ, 403, L21 (CM)
Chernin, L. M., Masson, C. R., Gouveia Dal Pino, E., & Benz, W. 1994, ApJ, 426, 204
Cummins, S., Linke, R., & Thaddeus, P. 1986, ApJS, 60, 819
Edwards, S., & Snell, R. L. 1983, ApJ, 270, 605
Gaume, R. A., Johnston, K. J., & Wilson, T. L. 1992, ApJ, 388, 489
Gottlieb, C. A., Gottlieb, E. W., Litvak, M. M., Ball, J. A., & Penfield, H. 1978, ApJ, 219, 77
Hartquist, T. W., Oppenheimer, M., & Dalgarno, A. 1980, ApJ, 236, 182
Kitamura, Y., Kawabe, R., Yamashita, T., & Hayashi, M. 1990, ApJ, 363, 180
Lis, D. C., Carlstrom, J. E., & Phillips, T. G. 1991, ApJ, 370, 583
Liseau, R., Sandell, G., & Knee, L. B. G. 1988, A&A, 192, 153
Margulis, M., Lada, C. J., & Snell, R. 1988, ApJ, 333, 316
Martin-Pintado, J., Bachiller, R., & Fuente, A. 1992, A&A, 254, 315
Masson, C. R., & Chernin, L. M. 1993, ApJ, 414, 230
Mezger, P. G., Chini, R., Kreysa, E., Wink, J. E., & Salter, C. J. 1988, A&A, 191, 44
Mitchell, G. F. 1984, ApJ, 287, 665
Moriarty-Schieven, G. H., & Snell, D. L. 1988, ApJ, 332, 364
Plambeck, R. L., Wright, M. C. H., Welch, W. J., Bieging, J. H., Baud, B., Ho, P. T. P., & Vogel, S. N. 1982, ApJ, 259, 617
Pineau des Forêts, G., Roueff, E., Shilke, P., & Flower, D. R. 1993, MNRAS, 262, 915 (PDFRSF)
Raga, A., & Cabrit, S. 1993, A&A, 278, 267
Richer, J. S., Hills, R. E., & Padman, R. 1992, MNRAS, 254, 525
Russell, A. P., Hills, R. E., & Padman, R. 1987, MNRAS, 226, 237
Rydbeck, O. E. H., Irvine, W. M., Hjalmarson, A., Rydbeck, G., Ellder, J., & Kollberg, E. 1977, ApJ, 215, L35
Snell, R. L., & Schloerb, P. 1985, ApJ, 295, 490
Snell, R. L., Scoville, N. Z., Sanders, D. B., & Erickson, N. R. 1984, ApJ, 284, 176
Stahler, S. 1993, in Astrophysical Jets, ed. M. Livio, C. O'Dea, & D. Bugarella (Cambridge Univ. Press)
Strom, K. M., Strom, S. E., & Vrba, F. J. 1976, AJ, 81, 308
Sutton, E. C., Blake, G., Masson, C. R., & Phillips, T. G. 1985, ApJS, 58, 341
Sutton, E. C., Danchi, W. C., Jaminet, P., & Blake, G. 1992, ApJS, 77, 255
Swade, D. 1989, ApJS, 71, 219
Welch, W. J., Wright, M. C. H., Plambeck, R. L., Bieging, J. H., & Baud, B. 1981, ApJ, 245, L87
White, G. J., & Phillips, J. P. 1981, MNRAS, 194, 947